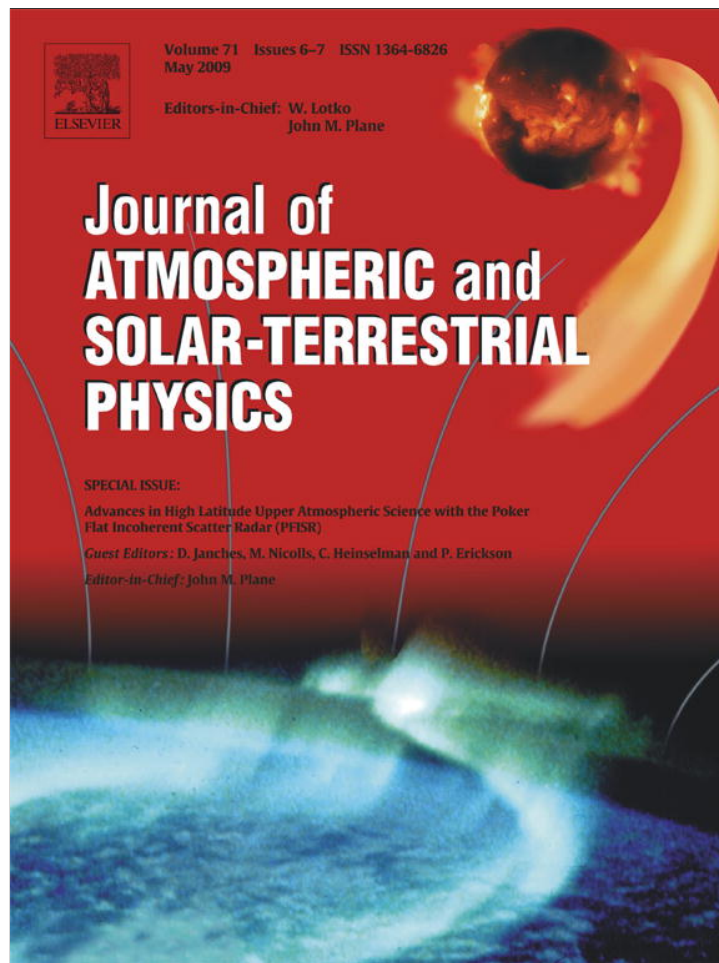


Provided for non-commercial research and education use.
Not for reproduction, distribution or commercial use.



This article appeared in a journal published by Elsevier. The attached copy is furnished to the author for internal non-commercial research and education use, including for instruction at the authors institution and sharing with colleagues.

Other uses, including reproduction and distribution, or selling or licensing copies, or posting to personal, institutional or third party websites are prohibited.

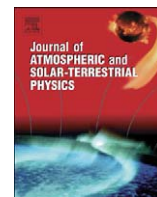
In most cases authors are permitted to post their version of the article (e.g. in Word or Tex form) to their personal website or institutional repository. Authors requiring further information regarding Elsevier's archiving and manuscript policies are encouraged to visit:

<http://www.elsevier.com/copyright>



Contents lists available at ScienceDirect

Journal of Atmospheric and Solar-Terrestrial Physics

journal homepage: www.elsevier.com/locate/jastp

Spectral observations of polar mesospheric summer echoes at 33 cm (450 MHz) with the Poker Flat Incoherent Scatter Radar

Michael J. Nicolls^{a,*}, Michael C. Kelley^b, Roger H. Varney^b, Craig J. Heinselman^a^a Center for Geospace Studies, SRI International, 333 Ravenswood Avenue, Menlo Park, CA 94025, USA^b School of Electrical and Computer Engineering, Cornell University, 320 Rhodes Hall, Ithaca, NY 14853, USA

ARTICLE INFO

Article history:

Accepted 17 April 2008

Available online 10 May 2008

Keywords:

Polar mesospheric summer echoes (PMSE)
Poker Flat Incoherent Scatter Radar (PFISR)
Ionospheric irregularities
Ionosphere/atmosphere interactions

ABSTRACT

In this paper, we report on multi-beam spectral observations of polar mesospheric summer echoes (PMSE) at 450 MHz (Bragg scattering wavelength of ~ 33 cm) carried out with the Poker Flat Incoherent Scatter Radar (PFISR) located near Fairbanks, Alaska. The observations presented in this paper occurred with auroral particle precipitation, which enhanced the otherwise low nighttime *D*-region ionization. The observations indicate two classes of spectra associated with PMSE at this frequency: a relatively rare, “broad” class of spectra that seems to be particularly turbulent with spectral widths (root mean square velocity fluctuations) of 6–7 m/s, and the more common “narrow” spectra, with spectral widths close to 1 m/s. The results are discussed in terms of the turbulence scattering theory of PMSE. Using the theories of Rapp and Lübken [2003. On the nature of PMSE: electron diffusion in the vicinity of charged particles revisited. *Journal of Geophysical Research* 108, 8437, doi:10.1029/2002JD002857], we find that neutral turbulence together with enhancement of the Schmidt number by the presence of charged ice can indeed explain the observations, even at these small scales. The echoes are likely associated with large charged ice particles (a few 10s of nanometers in radius). The narrowest echoes, while seemingly resulting from relatively modest neutral turbulence, thus acquire long diffusion times which allow them to drift with the background winds for tens of seconds, possibly explaining the predominance of these narrow-width echoes.

© 2008 Elsevier Ltd. All rights reserved.

1. Introduction

Polar mesospheric summer echoes (PMSE) are radar returns from the region around the cold summer mesopause (Cho and Kelley, 1993; Cho and Röttger, 1997; Rapp and Lübken, 2004), first reported in the early 1980s (Czechowsky et al., 1979; Ecklund and Balsley, 1981; Balsley et al., 1983). The polar summer mesopause is host to the coldest temperatures on Earth, with mean temperatures near 130 K (e.g., Lübken, 1999), which allow for the growth of ice particles despite very low water vapor concentrations. The prevailing explanation for PMSE centers around the neutral air turbulence that is known to be fairly common in the region, resulting from gravity wave breaking (e.g., Garcia and Solomon, 1985). This neutral turbulence has inner scales of meters and cannot generate the necessary irregularities at typical radar probing frequencies of tens or hundreds of MHz by using Kolmogorov energy dissipation arguments. To overcome this difficulty, it was postulated that the dissipation rate of electron density fluctuations would be slower than the dissipation rate of energy because of reduced electron diffusion (Kelley et al., 1987;

Cho et al., 1992a). This reduced diffusion could result from charged ice particles (or heavy ion clusters), which act as a “brake” on the electrons through ambipolar forces (e.g., Cho et al., 1992a; La Hoz et al., 2006). Such effects are controlled by the Schmidt number, which is the ratio of neutral viscosity to plasma diffusion coefficients (with the former controlling the dissipation of energy, and the latter controlling the dissipation of electron density fluctuations). The presence of charged aerosol particles has been proven by rocket measurements of electron density depletions at PMSE altitudes (Pedersen et al., 1969; Ulwick et al., 1988), which occur as a result of electron attachment to the aerosol particles (e.g., Reid, 1990), as well as more recent direct measurements of the particles themselves (Havnes et al., 1996; Mitchell et al., 2001).

It was quickly realized that this theory had problems, after the results of Cho et al. (1992a) showed that a significant amount of the free charge must be tied up in the aerosol (charged ice) particles for the theory to work. In fact, Cho et al. (1992a) found that this factor, $|Z_A|N_A/N_e$, must be at least 1.2 for Z_A negative (negatively charged ice). Given expected densities of charged ice, this would imply charge numbers of several hundred for some observations (e.g., Cho et al., 1992b). These results led Cho and Röttger (1997) to conclude that neutral turbulence could not be the dominant generation mechanism of PMSE, since observed

* Corresponding author. Tel.: +1 650 859 4813.

E-mail address: michael.nicolls@sri.com (M.J. Nicolls).

spectral widths were too narrow (implying Schmidt numbers that appeared to be far too high). In addition, some observations also showed that neutral air turbulence did not always occur in the same volume as PMSE (Lübken et al., 1993, 2002), which seemed to preclude the mechanism as the driver. Furthermore, an observed anticorrelation between power and spectral width seemed to preclude turbulence as the driver, since one would expect these two quantities to correlate (as larger spectral widths imply larger turbulence energy dissipation rates) (e.g., Röttger and La Hoz, 1990).

Recently, however, theoretical advances by Hill et al. (1999) and Rapp and Lübken (2003) have seemed to overcome the difficulties of the Cho et al. (1992a) theory. Hill et al. (1999) point out that the effective electron diffusion coefficient of Cho et al. (1992a) can only apply if all ion species have the same diffusion coefficient, a condition that is not met. The Rapp and Lübken (2003) theory, different from the Cho et al. (1992a) theory because of an initial condition assuming spatially anticorrelated negatively charged aerosol particles and electrons, does not have the strong dependence on $|Z_A|N_A/N_e$, and in fact finds that the electron diffusion rate can be reduced for all reasonable values of that parameter. In turn, this seems to be more consistent with observations, which show indeed that PMSE occur with $|Z_A|N_A/N_e \ll 1$ (Rapp et al., 2003). Furthermore, Rapp and Lübken (2003) point out that the reduced diffusion rate allows the electron density irregularities to acquire a long diffusion time, thus decoupling the existence of active air turbulence from PMSE. Other features, such as narrow spectral widths, are also explained qualitatively. Direct numerical simulations of turbulence (Werne and Fritts, 1999; Gibson-Wilde et al., 2000) also showed that an anticorrelation between spectral width and echo power should be expected (Rapp and Hoppe, 2006). Thus, neutral turbulence has returned again as the most likely candidate for PMSE generation at all scales.

Observations of PMSE at the smallest scales (highest probing frequencies), of which there are only a few, have been summarized by La Hoz et al. (2006). Röttger et al. (1990) reported simultaneous observations of PMSE with the EISCAT UHF (930 MHz) system and a 46.9 MHz system. They estimated the turbulence energy dissipation rates from the scattering cross section and spectral widths, finding values of several hundred mW/kg. The authors found that it was difficult to explain observations at both frequencies from a single source, concluding that extension of the inertial-convective subrange of neutral turbulence to UHF Bragg scales was unlikely. The spectral observations of La Hoz et al. (2006) using the EISCAT UHF system found equivalent turbulence energy dissipation rates of 30–500 mW/kg (corresponding to rms velocity fluctuations of 2–8 m/s). A detailed analysis by La Hoz et al. (2006) concluded that no theory could adequately explain the observations at the smallest Bragg scales, unless the Schmidt number was enhanced by highly charged (charge numbers of 10–100) ice particles, for which there is little experimental evidence (e.g., Rapp and Lübken, 2001). However, as we will investigate later, La Hoz et al. (2006) assumed ice particle radii of 10 nm; larger particles can lead to higher Schmidt numbers (Cho et al., 1992a; Rapp and Lübken, 2003, 2004; La Hoz and Havnes, 2007; Rapp et al., 2008). The one observation of PMSE with the Sondrestrom incoherent scatter radar at 1.29 GHz by Cho et al. (1992b) implied a Schmidt number of ~ 5000 . Cho et al. (1992b) concluded that this would require such large particles and charge numbers as to be unexplainable by turbulence theories. PMSE at a frequency of 500 MHz have been measured by the EISCAT Svalbard radar (Hall and Röttger, 2001), but appears to be relatively rare (or difficult to measure, possibly as a result of ground clutter), as only a few measurements appear in the literature. If indeed rare, this could be the result of the low

D-region ionization in the polar cap that results from the high solar zenith angle (e.g., Varney et al., 2008)—it is well known that a minimum electron density is needed for PMSE to occur (e.g., Rapp et al., 2002). Thus, to date, the few observations of PMSE at the smallest scales remain unexplained—although we emphasize that most have been interpreted with the Cho et al. (1992a) theory, prior to the work of Rapp and Lübken (2003), which required a large fraction of the charge to be tied up in the ice particles. In addition to the aforementioned UHF systems, it is worth mentioning that PMSE is frequently measured with the EISCAT 224-MHz VHF system (e.g., Hoppe et al., 1988; Röttger et al., 1988), where spectral widths in the range 1–10 m/s are observed. Finally, we note that a recent study (Rapp et al., 2008) has investigated PMSE at three different frequencies, 53.5, 224, and 930 MHz, and has found consistency with turbulence scattering theory.

In this paper, we report on spectral observations of PMSE with the Poker Flat Incoherent Scatter Radar (PFISR), which operates at ~ 450 MHz (33 cm Bragg wavelength), about midway between the scales to which the EISCAT VHF and UHF systems are sensitive. Previous observations of PMSE by PFISR have been reported by Nicolls et al. (2007), who utilized PMSE backscatter power returns from multiple look directions to investigate the aspect sensitivity and layering characteristics of PMSE. A statistical study by Varney et al. (2008) has investigated the frequency of occurrence of PMSE at 33 cm during the summer of 2007.

2. Experiment description

PFISR is located at the Poker Flat Research Range (65.13°N, 147.47°W) near Fairbanks, Alaska. PFISR has the ability to steer on a pulse-to-pulse basis, providing a powerful extension over typical ISRs. The radar is tilted so that its boresight direction corresponds to elevation and azimuth angles of 74° and 15°, respectively. The beamwidth of the initial PFISR configuration (applicable to the data reported here) was about $1^\circ \times 1.5^\circ$, with the larger dimension in the plane perpendicular and north to the radar face. The experimental configuration used here employed five beam positions at a range of pointing angles centered around the boresight direction. The azimuths and elevations of the five beams are shown in Fig. 1 along with the latitude and longitude coverage of the beams from 60–90 km. Beam 3 is pointed vertically, beam 1 is pointed $\sim 10^\circ$ to the north, beam 4 is pointed $\sim 5^\circ$ to the east, beam 2 is pointed $\sim 10^\circ$ to the west, and beam 5 is pointed $\sim 5^\circ$ to the south.

The experimental mode consisted of transmitting $10 \mu\text{s}$ (1.5 km), 13-baud Barker-coded pulses on two frequencies (449.3 and 449.6 MHz) sampled at $5 \mu\text{s}$ with an IPP of 4 ms (600 km in range). The available duty cycle of the system is close to 10%. One hundred and twenty-eight pulses were transmitted in each direction before switching the look directions, and pulse-to-pulse autocorrelation functions (ACFs) were computed, which were then transformed to power spectral estimates. Computing ACFs instead of spectra directly from the samples was done because it allows for the handling of “missed” pulses (sequences of less than 128 pulses), allows for arbitrary windowing of the ACF (and direct removal of the intrinsic triangular weighting if desired), and also allows for twice the frequency resolution by assuming that the ACF is symmetric (that the power spectrum is real). Two full cycles (ideally 256 pulses in all five directions) were completed before writing the raw data to disk. These experimental parameters allow for a highest frequency resolution of 0.98 Hz (0.33 m/s), and a full spectral width of at most 250 Hz (83.75 m/s). At the full Doppler resolution, the highest spectral time resolution is 2.5 s, although this can be improved if frequency resolution is

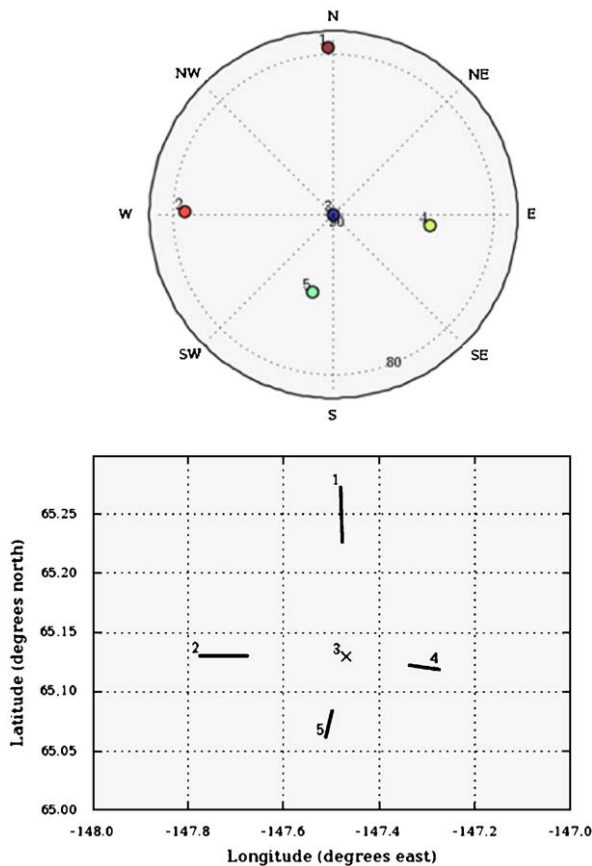


Fig. 1. (Top) Azimuth and elevations of the five beams used for this experiment. (Bottom) Latitude and longitude coverage for altitudes from 60 to 90 km.

sacrificed. We note that the effects of beam broadening are quite small, at most 1–2 Hz, given the narrow beam and frequency of PFISR (e.g., Hocking, 1985). Noise estimates were obtained from ranges below those of interest but above contaminating ground and tropospheric clutter sources, from 55 to 65 km. Received power was calibrated to absolute volume reflectivity on each frequency using injected calibration pulses from a previous experiment and a system constant approach as described by Nicolls et al. (2007).

The experiments described in this paper were run in August 2007. At that time, PFISR consisted of 96 transmit and receive panels, with an average transmit power for these experiments of ~ 1.2 MW. The mode was run from 1 to 14 August 2007 from 11–19 UT (02–10 AKST). Other measurements were also taken during this time period, including incoherent “imaging” observations (Nicolls et al., 2007), lidar measurements, and optical camera measurements. For the purposes of this paper, we will focus on the spectral observations on the night of 10–11 August.

3. Observations

Fig. 2 shows the calibrated reflectivity measured by PFISR in all five look directions on the night of 10–11 August 2007. These power measurements have a time resolution of approximately 5 s, corresponding to ~ 256 individual power measurements. Intense auroral particle precipitation is evident from the start of the experiment, with significant ionization peaking in the altitude range ~ 90 – 95 km beginning at about 1230 UT. PMSE is evident as the layer of enhanced backscatter near ~ 80 – 85 km. The PMSE is

visible in all five beams with roughly consistent trends: a weak scattering layer until ~ 1230 UT, enhanced backscatter for 2–3 h until after 1500 UT, and a resurgence near 1800 UT. Such strong general coherency in the observations strongly suggests a broad scattering layer encompassing all beams (a roughly 30×30 km region at 80 km). This is consistent with the previous observations with PFISR by Nicolls et al. (2007). The strongest PMSE occurs just before 14 UT where the sidelobes from the Barker decoding are evident. Note that there are methods to remove such artifacts using an unmatched filter (e.g., Sulzer, 1989; Lehtinen et al., 2004), however, for this processed data we did not employ these schemes because of increased difficulty in obtaining good noise estimates. The upper right panel of Fig. 2 shows a zoomed-in version of this last patch of PMSE, where layer descent is clearly evident.

Despite the broad general beam-to-beam coherency in the power observations, there is significant beam-to-beam structure in the observations, which will be discussed shortly. In addition, the spectral characteristics of the scatterers change strongly as a function of time, even within the same “patch” of PMSE. Fig. 3 shows spectra as a function of time for the vertical beam only at a single altitude (centered at 82.2 km) for the time period from 1320 to 1510 UT, which includes the strongest echoes (with reflectivities $> 10^{-15} \text{ m}^{-1}$). Each row in this figure represents an ~ 18 -min time period, with the color plots showing the spectra at the full time resolution (each color image is individually scaled), and the line plots showing ~ 1.2 -min integrated (averaged) spectra, each of which is individually scaled. The spectra have been computed for each transmission frequency at their full Doppler resolution, combined with a running median for 15 s (corresponding typically to six spectral estimates), calibrated and scaled according to the different gains of the two receiving channels, and then the two independent estimates (two transmission/reception frequencies) combined together to form the spectral estimate. The estimates from the two different frequencies were examined independently and were found to be very consistent with each other, implying a strong coherent scattering mechanism for much of the echoes.

The echoes in Fig. 3 show a dramatic range of behavior. Initially, the echoes are quite weak, spectrally extremely narrow, and show some interesting characteristics, such as a clear double peak at ~ 1330 – 1335 UT. This double peak could be associated with a Kelvin–Helmholtz roll occurring with the beam; however, we will not discuss these possibilities or these spectral features in this paper. The second panel shows enhanced echoes, spectrally quite narrow (a few Hertz), with smooth trends indicating a stable source drifting with a background field. The magnitude of this drift is a few meters per second and shows periodicities at the several-minute time scale. Later, after 1445 UT, the echo characteristics change abruptly from the narrow features to much broader returns, on the order of 10–20 Hz. These echoes are much less regularly behaved than the previous echoes, showing very short time-scale variations. Note that while the earlier echoes may look broad on the log-scale color plot, this is partly because they are so strong; the line spectra (right panels) show that they are in fact quite narrow as compared to the broader, more turbulent echoes in the lower panels. It is tempting to suggest that the ~ 18 -min quasi-sinusoidal variations in panels 2–4 of Fig. 3 (and in all beams at those times, as seen in Fig. 4) are due to a gravity wave that within the next half hour broke and induced the very turbulent echoes observed in panel 6.

Information on the beam-to-beam variability of the echoes is shown in Fig. 4, where we plot the spectral estimates from two 18-min time periods for all five beams at an altitude close to ~ 82 km. The left panels show examples of spectrally narrow echoes whereas the right panels show examples of broader echoes. The broad echoes are far more turbulent and structured than the narrow echoes, a trend seen consistently throughout the data set.

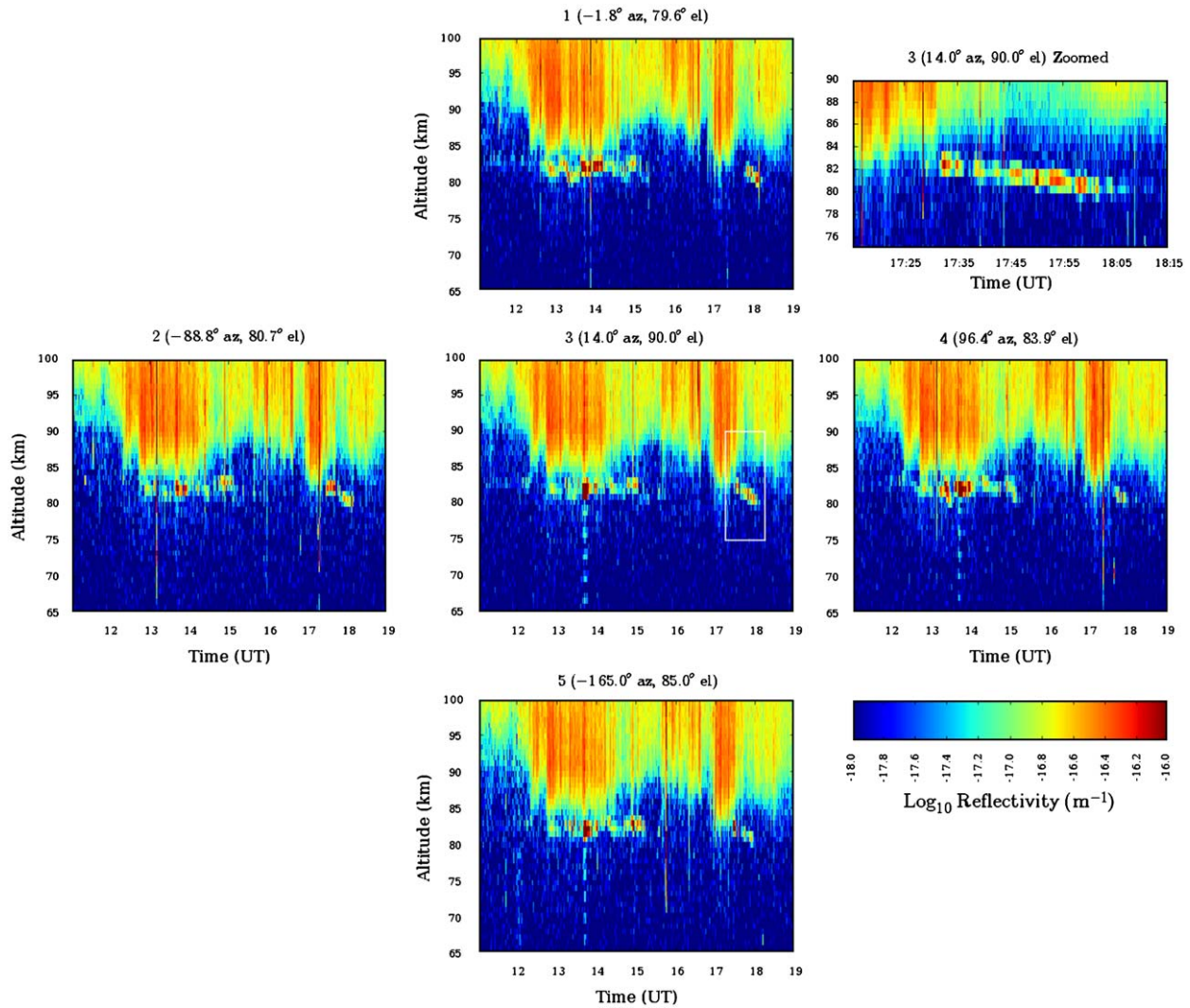


Fig. 2. Reflectivity measured in five look directions by PFISR for the night of 10–11 August 2007. The upper right panel shows a zoomed-in version of the white-boxed region of the vertically looking beam.

The narrow echoes follow regular neutral wind trends, whereas the Doppler velocities from the broad echoes fluctuate significantly. In the westward (lowest elevation angle) pointing beam, the mean Doppler for this period is in excess of 75 Hz. If interpreted in terms of horizontal neutral motions, this corresponds to winds of ~ 150 m/s. However, there is no doubt that there is significant spatial variability in these Doppler velocities; for example, note the transition from negative to positive Dopplers in the southward pointing beam after 1500 UT, which is not seen in the northward pointing beam. The northward pointing beam also exhibits smaller mean Dopplers, despite the fact that this beam is pointed at a lower elevation angle than the southward pointing beam. The vertical drifts of several meters per second are consistent with other observations in the polar summer mesopause (e.g., Fritts et al., 1990).

In order to examine more quantitatively the spectral widths and Dopplers of the observed echoes, we have fitted the processed spectra with a Gaussian shape. Note that for a Gaussian, the half-power half-width is related to the standard deviation by the expression $HPHW = \sigma_f \sqrt{2 \ln 2}$. The Doppler velocities and Doppler spectral widths (the standard deviation from the Gaussian distribution, which we relate to the velocity variance of the scatterers) are plotted in Figs. 5 and 6 for the two time periods focussed on in Fig. 4. Background ionization and spectral features

from the aurorally induced particle precipitation are evident. The narrow echoes in Fig. 5 show strong returns from the vertically, eastward, and southward pointing beams, with the strong returns beginning overhead, implying a source region close to overhead and then drifting with the background winds, which are indeed southward (see Doppler from southward and northward pointing beams). A structure drifting with a wind of ~ 100 m/s would take just a few minutes to advect 15 km, consistent with observations. The background winds also appear to be westward, which does not explain why the echoes show up in the eastward beam and not the westward beams, perhaps implying a second source region. Looking at the spectral widths of the echoes, the strongest echoes here are the broadest, as the widths are close to 3 m/s at the beginning of the event, and narrow to < 1 m/s at about 13.8 UT. It is interesting that this reversal occurs with the reversal of the vertical drift from negative to positive. This effect could be due to the fact that vertically propagating waves are more likely to be convectively and/or dynamically unstable during their upward phase (e.g., Hoppe and Fritts, 1995), implying higher turbulence dissipation rates and corresponding vertical velocity variances. The strongest echoes here also occur with the most intense precipitation, which enhance the background density and density gradient, to which index of refraction variations are sensitive (e.g., Hocking, 1985; Rapp et al., 2008).

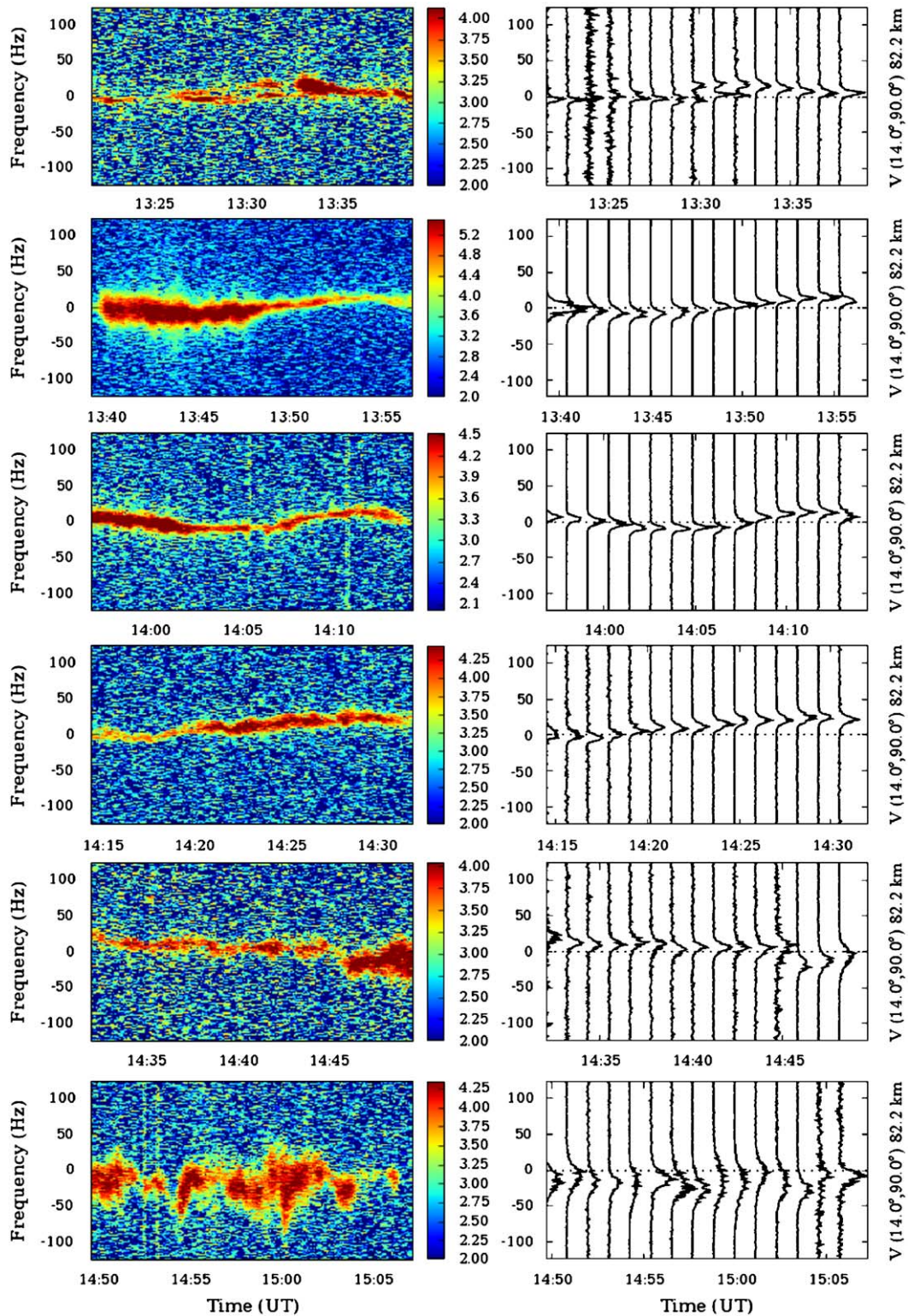


Fig. 3. Spectral estimates from the vertically looking beam for six different 20-min time periods. The left color plots show the \log_{10} of the calibrated spectral density as a function of time and frequency, at approximately 15-s resolution, with each time period on its own scale (see colorbars). The right plots show ~ 1.2 -min integrated spectra, with each line plot individually normalized, on a linear scale. The beam direction is denoted by vertically oriented text on the right-hand side of the figure.

The much broader echoes in Fig. 6 (with widths typically in the range 5–7 m/s, but often reaching over 10 m/s) tell a different story. These echoes are patchy from beam-to-beam and show no obvious drifting of irregularities from beam-to-beam. There is no obvious meridional flow pattern, as the north and south-looking

beams observe very different Doppler trends—while the northward-looking beam observes predominantly negative (southward flows), the southward-looking beam's Doppler fluctuates by tens of meters per second (if interpreted as horizontal motion, 100–200 m/s fluctuations in the meridional neutral wind in a

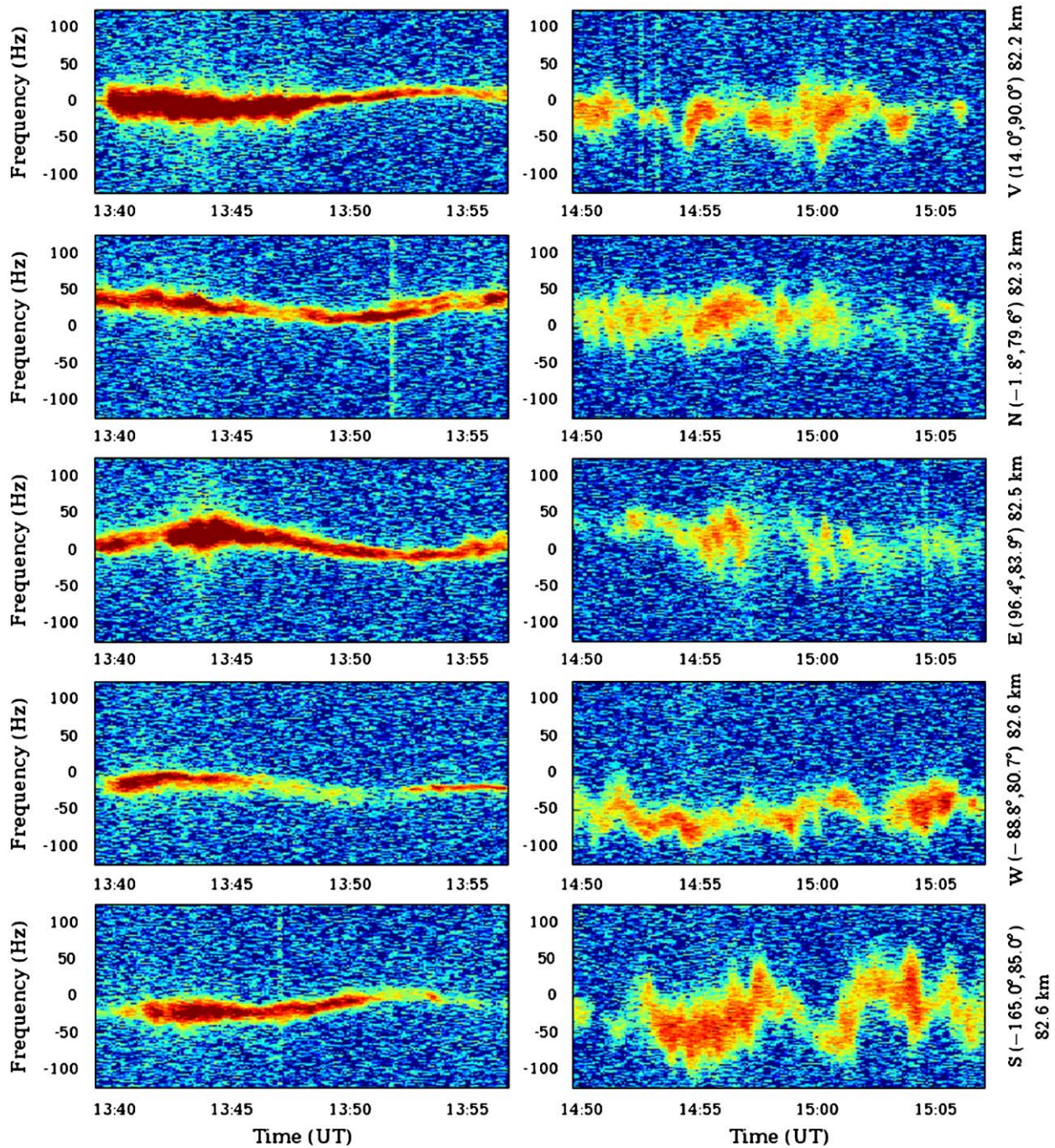


Fig. 4. Spectral estimates from all five beams (rows) for two different 18-min time periods (columns) at a single altitude. All panels are on the same color scale. The beam direction is denoted by vertically oriented text on the right-hand side of the figure.

span of a few minutes). The zonal flow is somewhat more regular, with predominantly westward flows, however, the westward-looking beam observes significantly larger Dopplers (but roughly consistent with the different elevation angles of the two beams if the motion is predominantly horizontal). The vertical velocity fluctuations are also significant, with Dopplers varying from 0 to 10 m/s, predominantly upward, with the larger Dopplers corresponding to stronger and broader echoes. These observations seem to imply measurement of PMSE during an actively turbulent environment, in juxtaposition to the “narrow echo” observations of Fig. 5.

Fig. 7 summarizes the observed spectral widths on this night, showing histograms of the observed widths, where we have

included only echoes with SNRs > -4 dB and reflectivities > 10^{-17} m^{-1} . The spectra have been fitted at the highest time and spectral resolution. The echoes from all altitudes show a peak at very narrow widths, which may be interference/noise spikes on top of the broad incoherent scatter echoes at higher altitudes, a peak near 1–1.5 m/s, and a peak at broader widths, which is incoherent scatter from the higher altitude echoes. The histograms from altitudes in the range 80–84 km reveal the distribution of spectral widths associated with PMSE. Most of the echoes are spectrally quite narrow, with a peak in the distributions, from all beams, at just over 1 m/s. The consistency of the results from beam-to-beam implies that beam broadening was not important, even for the off-zenith directions. The broad

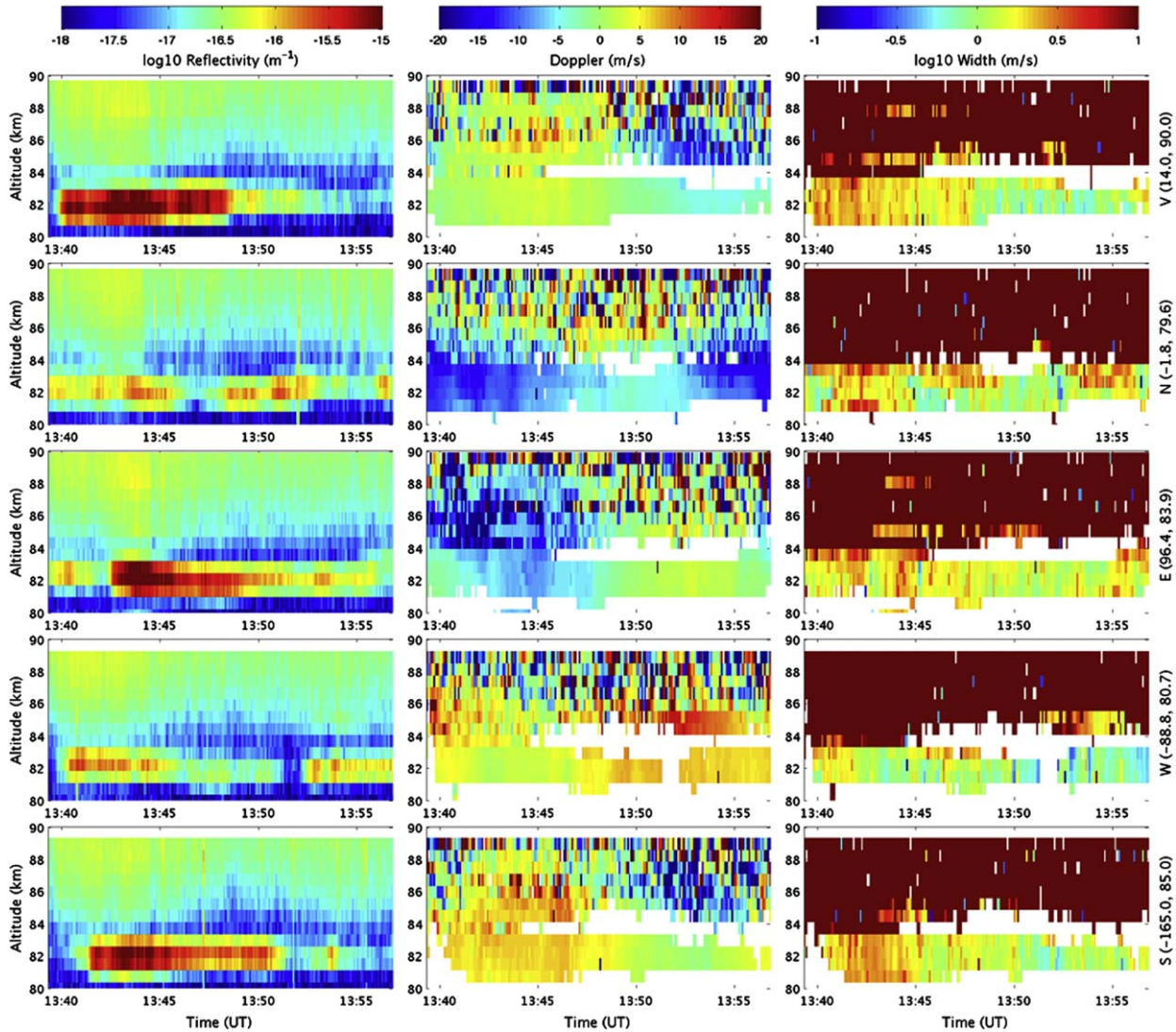


Fig. 5. Volume reflectivity (m^{-1} , on a log scale), Doppler velocity (m/s), and rms spectral width (m/s, on a log scale) as a function of altitude and time for all five beams for a “narrow” echo time period. The beam direction is denoted by vertically oriented text on the right-hand side of the figure.

echoes (spectral widths > 5 m/s) occur far less regularly in this data set. The beam-to-beam histograms are remarkably well-behaved, but do show some interesting differences. First, there are more echoes, especially narrow echoes, towards the north (and the fewest number of echoes towards the south), which may indicate that the generating mechanism (i.e., ice particles, or the presence of sufficient ionization) are more predominant towards the north. Note that there is a potential instrumental effect here, as the radar is more sensitive in its boresight direction, which is towards the north, but this has been accounted for by calibration and a filtering of echoes by minimum reflectivity. Second, there are some small differences in histogram shape; however, we hesitate drawing too much into these as this paper includes observations for only one day of measurements.

4. Discussion

4.1. Evaluation of turbulence parameters

The most likely explanation for the existence of PMSE at Bragg scales of meters to centimeters is the generation of irregularities by neutral turbulence (e.g., Rapp and Lübken, 2004). If this is the

case, then the turbulent driver will affect the root mean square fluctuating velocity of the scatterers and the spectral width of the received signal will then be a measure of the turbulence energy dissipation rate (e.g., Hocking, 1983, 1985). The spectral width (standard deviation of the Gaussian spectral fit) is the square root of the velocity variance of the scatterers which, if purely due to turbulent motions, can be related to a turbulent energy dissipation rate by Hocking (1985)

$$\varepsilon \approx C \sigma_v^2 \omega_B \times 1000 \approx 9.8 \sigma_v^2 \text{ mW/kg} \quad (1)$$

where we have used a value for C of 0.47 (Weinstock, 1981; Hocking, 1996) and a Brunt–Vaisala period of 5 min, which was used by Hocking (1988) and La Hoz et al. (2006). Note that direct numerical turbulence simulations by Gibson-Wilde et al. (2000) have suggested that computation of the turbulent energy dissipation rate in the manner above may result in an underestimate by a factor up to ~ 5 , although recent results (e.g., La Hoz et al., 2006; Rapp et al., 2008) have continued to use values of C of 0.4–0.5.

The peak in the velocity standard deviation plot of Fig. 7 implies turbulence energy dissipation rates of $\sim 1\text{--}3 \times 10^{-2}$ W/kg, somewhat similar to the EISCAT VHF (224 MHz) observations of Röttger et al. (1988) and the EISCAT UHF (933 MHz)

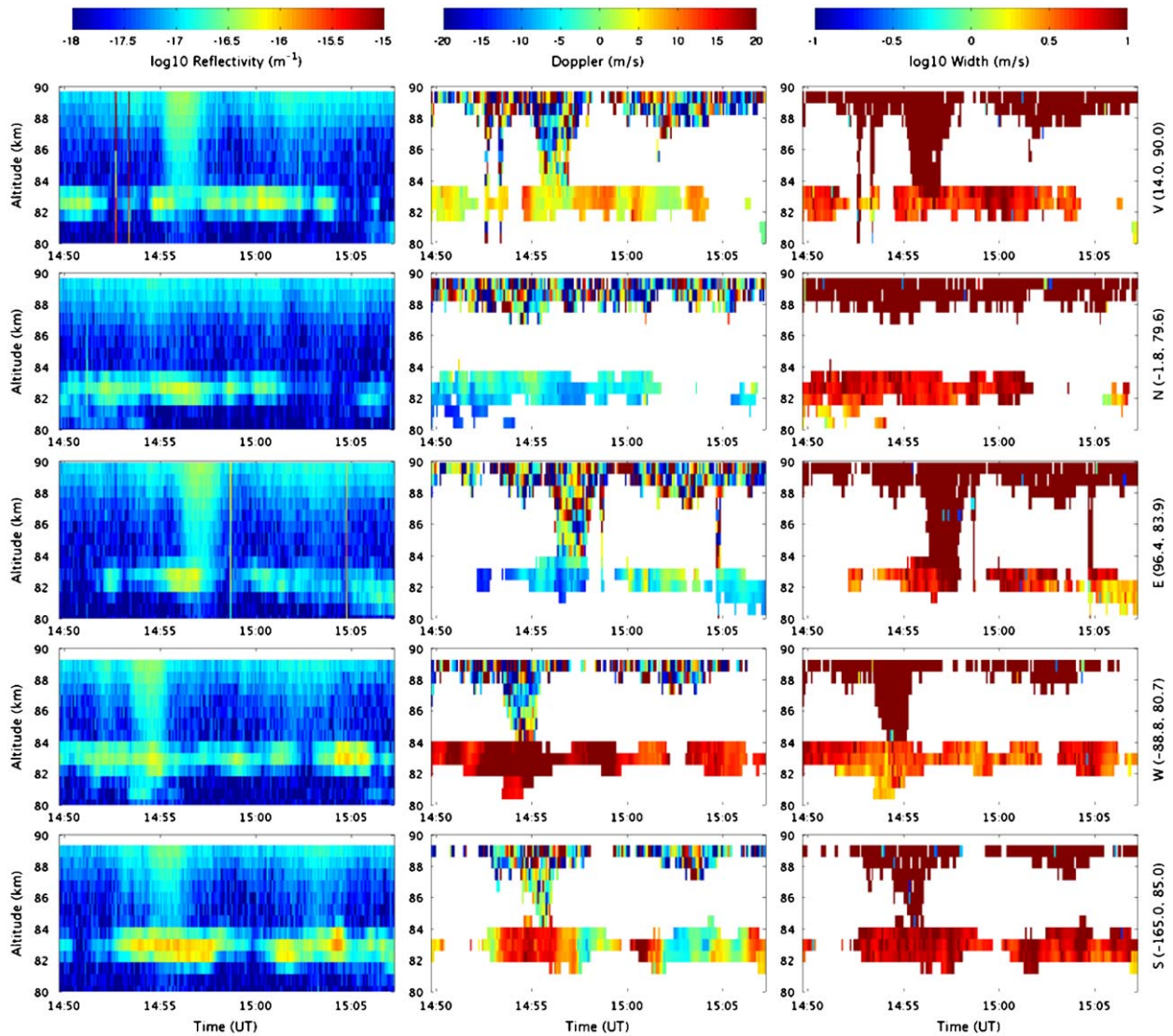


Fig. 6. Same as Fig. 5 for the “broad” echoes.

observations of Röttger et al. (1990) and La Hoz et al. (2006). These very low energy dissipation rates imply weak to moderate turbulence, well within measurements of turbulence energy dissipation rates (e.g., Lübken, 1997; Lübken et al., 2002). The spectral widths, then, are consistent with turbulence as a generation mechanism, however, the existence of echoes at a Bragg scattering wavelength of 33 cm is not. One might think that observations at the highest frequencies (hundreds of MHz) could only occur in the presence of extremely intense turbulence, which would imply broad spectra (around 15 m/s, which would correspond to the highest measured turbulence dissipation rates near 2.5 W/kg, Lübken et al., 2002; Rapp and Lübken, 2004). However, this is clearly not the case, implying that, if indeed turbulence is the causative mechanism, another effect plays a more dominant role, if weak to moderate turbulence is able to drive irregularities at the smallest scales.

As outlined in the introduction, turbulence has an inner scale of several meters, so to extend the inertial subrange of neutral turbulence to UHF scattering wavelengths requires a slowing of electron diffusion relative to that of the neutrals (which diffuse as a result of viscosity). This slowing is defined in terms of the Schmidt number, which is the ratio of the two diffusion

coefficients,

$$Sc = \frac{\nu_a}{D_e} \quad (2)$$

where ν_a is the coefficient of kinematic viscosity and D_e is the electron particle diffusion coefficient (e.g., La Hoz et al., 2006). The fact that some extension of the inertial subrange is necessary is evident by computing the Kolmogorov energy dissipation scale for the turbulence energy dissipation rate derived from the measurements presented earlier. The Kolmogorov microscale is given by (e.g., Hill and Clifford, 1978; Hocking, 1985)

$$\eta_k = \left(\frac{\nu_a^3}{\varepsilon} \right)^{1/4} \quad (3)$$

which has units of meters. We can associate this with a wavenumber, $k_{\eta_k} = \eta_k^{-1}$ (Rastogi and Bowhill, 1976), so that the corresponding radar Bragg wavelength is $\lambda_{\eta_k} = 2\pi\eta_k$, where the factor of 2π is important (e.g., La Hoz et al., 2006). To be a measure of the inner scale, this number needs to be scaled by at least a factor of 1.2–1.35 for density fluctuations (Rastogi and Bowhill, 1976; Hocking, 1985), further by a factor depending on the Prandtl number (ratio of momentum diffusion and temperature diffusion

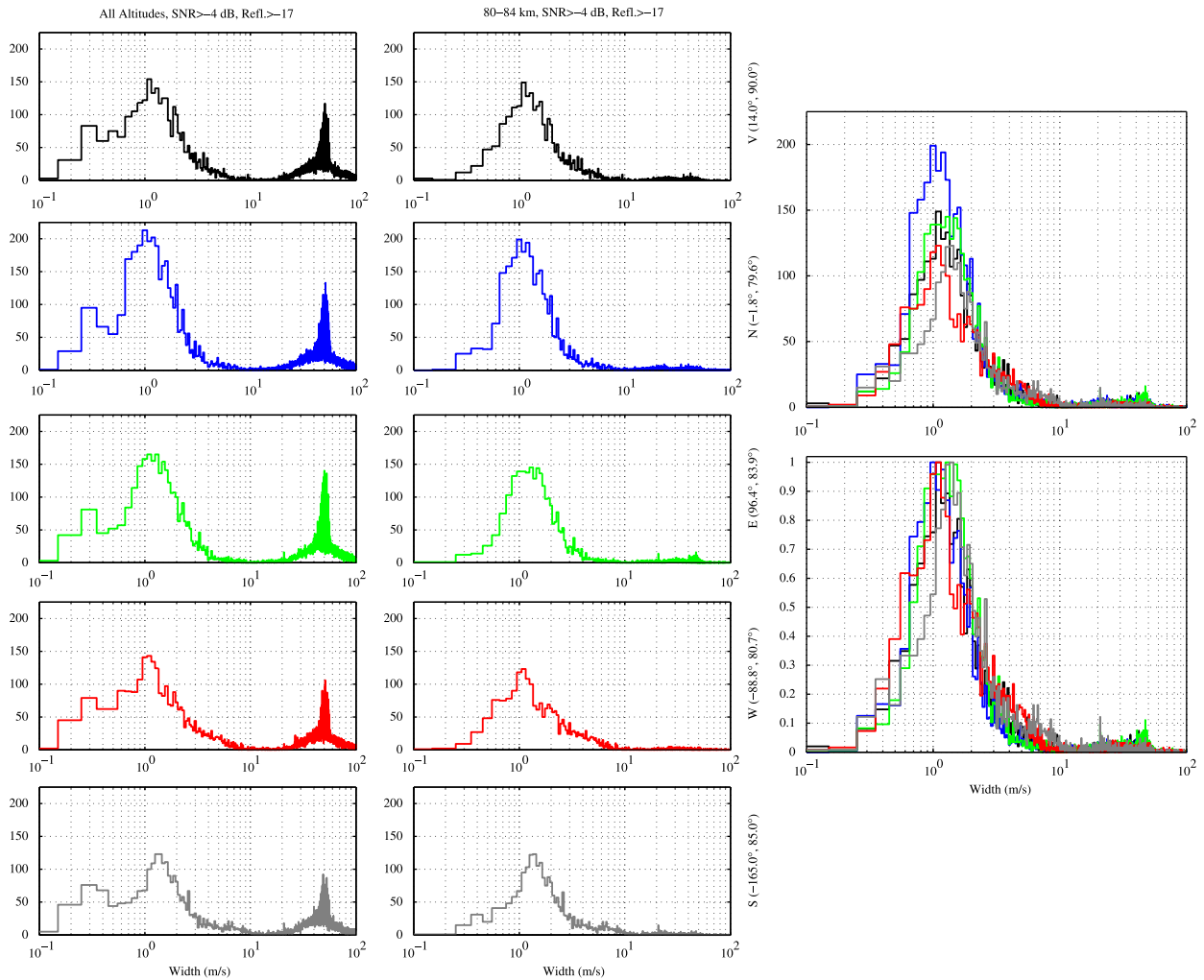


Fig. 7. Histograms of spectral widths (root mean square velocity fluctuations) for all five beams and all altitudes up to 90 km (left) and altitudes from 80 to 84 km. The plots on the right show the histograms on the same scale (top) and then normalized to their maximum value (bottom).

rates) for velocity fluctuations (Hocking, 1985), and then by a factor of 2–4 (Hocking, 1985; La Hoz et al., 2006) to represent the true break in slope from the inertial to viscous subranges. For our experimental results, we find using an MSIS neutral atmosphere (Hedin, 1991) that the neutral mass density is $\rho \approx 1.34 \times 10^{-8} \text{ g/cm}^3$, and taking $T_n \approx 150 \text{ K}$ yields $v_a = 0.87 \text{ m}^2/\text{s}$, so that $\eta_k \approx 2.86 \text{ m}$. This corresponds to a minimum Bragg wavelength of 18 m, corresponding to a probing frequency of $\sim 8 \text{ MHz}$. Again, for the Bragg scale to be in the inertial subrange, the Bragg wavelength needs to be additionally scaled by a factor of 2–4 (Hill and Clifford, 1978; Hocking, 1985; La Hoz et al., 2006).

Enhancement of the Schmidt number could occur as a result of the “braking” effects of massive charged particles, namely heavy ion clusters or charged ice, an idea first proposed by Kelley et al. (1987). As outlined by La Hoz et al. (2006), the electron irregularities can then be treated as a passive conserved scalar driven by the neutral turbulence, whose spectrum would then be Batchelor in shape (Batchelor, 1959). The Batchelor microscale is then

$$\eta_B = \left(\frac{v_a^3}{Sc^2 \varepsilon} \right)^{1/4} \quad (4)$$

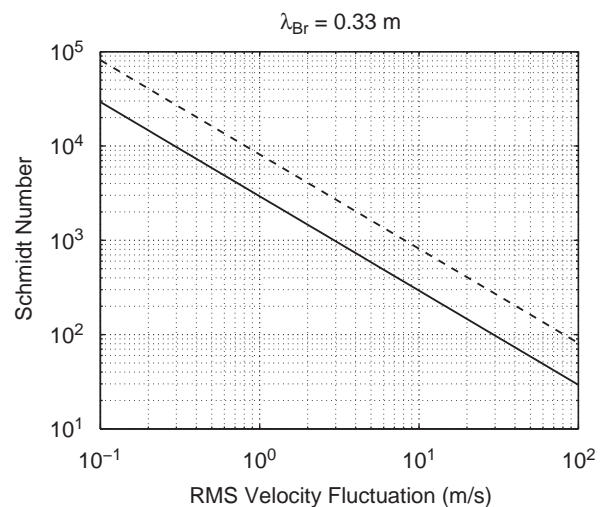


Fig. 8. Spectral width as a function of Schmidt number for a Bragg wavelength of 33 cm and $v_a = 0.87 \text{ m}^2/\text{s}$. The solid line shows the Batchelor scale and the dashed line shows the slightly modified scale of the inertial subrange proposed by La Hoz et al. (2006).

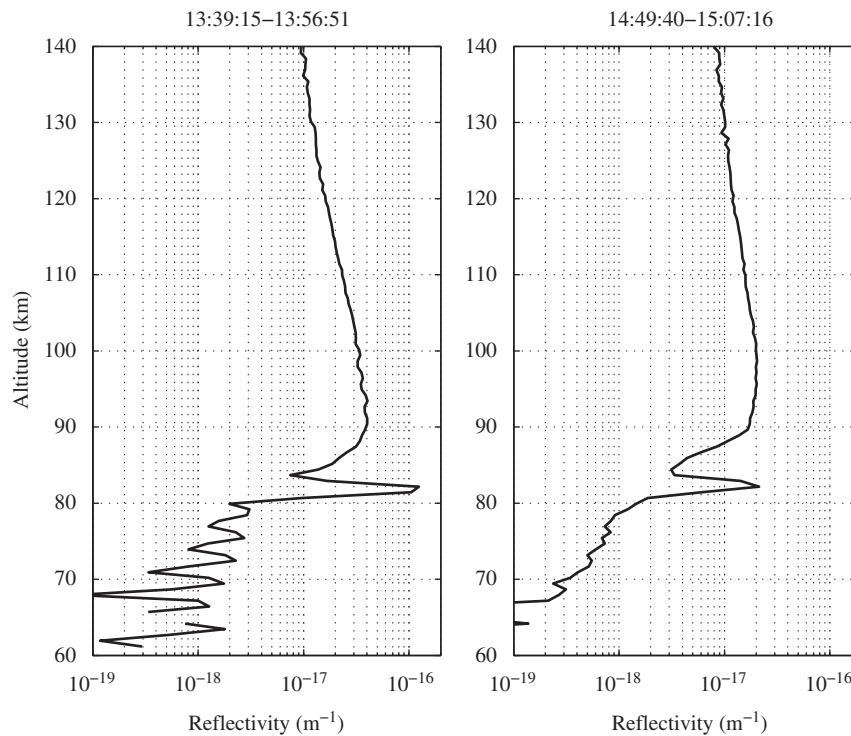


Fig. 9. Radar reflectivity as a function of altitude measured by the vertically looking beam for two different ~ 18 -min time periods. For reference, for incoherent scatter, reflectivities of 10^{-18} and 10^{-17} m^{-1} correspond to electron densities of $\sim 2 \times 10^{10}$ and 2×10^{11} m^{-3} , respectively.

where it is clear how enhancement of the Schmidt number extends the inertial-convective subrange. This can then be related to a Batchelor wavelength of $\lambda_{\eta_B} = 2\pi\eta_B$, as in the Kolmogorov case. Fig. 8 shows the necessary Schmidt number as a function of the rms velocity fluctuation (spectral width) for the PFISR Bragg wavelength of 33 cm. The solid line shows the result using the Batchelor scale above, whereas the dashed line is an analytical increase in the Batchelor scale by a factor of $\frac{5}{3}$ proposed by La Hoz et al. (2006), necessary because of the precipitous drop in spectral shape in the viscous-diffusive subrange. For spectral widths of ~ 1 m/s, we find that Schmidt numbers of at least 3000 are necessary, with up to almost 8000 using the stricter condition. These Schmidt numbers are similar to those derived from other UHF measurements (e.g., Cho et al., 1992b). In addition, we note that these numbers may in fact be overestimates; if the observed turbulence is fossilized (observed away from the generation region, or in the absence of neutral turbulence), then one would expect a reduction in the rms velocity fluctuations and a narrowing of the spectra (Rapp and Lübken, 2003). Thus, using the narrow widths as a measure of the turbulence dissipation rate results in an underestimate of that parameter, and an overestimate of the required Schmidt number. The broad spectra of Fig. 6 may be more representative, and have rms velocity fluctuations of closer to $\sigma_v \approx 5$ –7 m/s, corresponding to required Schmidt numbers of ~ 500 –1200.

With measurement of both the absolute reflectivity and the turbulence energy dissipation rate, the results can be compared directly to the Batchelor turbulence theory with only the Schmidt number as a free parameter. This approach has been used by Rapp et al. (2008), who derived an expression for the radar volume reflectivity in the viscous-convective subrange. This expression has many quantities that are uncertain, but depends critically on the radar refractive index, which is a function of the electron density and electron density gradient in the vicinity of the PMSE. Fig. 9 shows average reflectivity profiles for the two ~ 18 min time periods highlighted throughout the text. The first time period,

during which the narrow, extremely strong echoes were observed, shows a deep ledge with a peak in ionization down to about 90 km. PMSE occurred below the ledge where the electron density was still quite high (close to 10^{11} m^{-3}) and where the electron density gradient was quite large. In the second time period, during which the broader, more turbulent echoes occurred, the background densities were not as enhanced ($\sim 5 \times 10^{10}$ m^{-3}) and the gradients were not as large. These effects likely contributed to the fact that the echoes during the first time period were very intense. However, it is not the complete story, as often there is not such strong correlation between density and PMSE strength. In addition, we note that during precipitation events, the background density and gradient can change extremely rapidly. Nevertheless, using the above derived Schmidt numbers, and taking into account the uncertainty of many of the parameters, one can show that indeed the expressions of Rapp et al. (2008) for the volume reflectivity are roughly consistent with the measured reflectivities and turbulence energy dissipation rates.

4.2. Enhancement of the Schmidt number

The question now is whether Schmidt numbers of 3000–8000, or even 500–1200, are reasonable given reasonable polar summer mesopause conditions. This question has been investigated originally by Cho et al. (1992a), and more recently by Rapp and Lübken (2003) and La Hoz et al. (2006) as discussed in the introduction. These works are based on the Hill (1978) theory for ambipolar diffusion in a multi-component plasma. That theory yields two diffusion modes for a three component plasma that consists of (possibly multiply) charged ice particles, water cluster ions which are thought to be dominant in the region (Rapp and Lübken, 2001, 2003, 2004), and electrons. The water cluster ions have a diffusion coefficient dominated by a polarization interaction, which has been described by Cho et al. (1992a). The charged aerosols on the other hand are characterized by a hard sphere

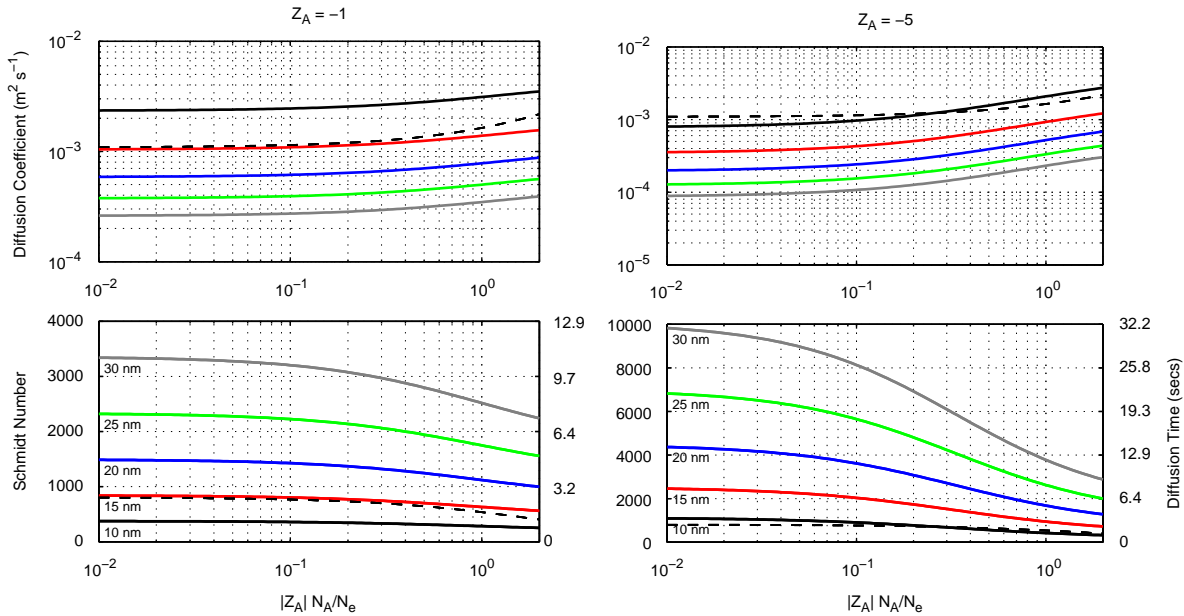


Fig. 10. (Top panels) “Slow” diffusion coefficient as a function of the fraction of charge held in the ice particles, $|Z_A|N_A/N_e$ for various particle sizes, denoted in the bottom panel. (Bottom panels) Schmidt number (left axes) and slow diffusion times (right panel) for the same particle sizes. The dashed line corresponds to the “fast” diffusion coefficient, divided by a factor of 1000 in the top panel and multiplied by a factor of 1000 in the bottom panel. Ice particle charge number of $Z_A = -1$ and -5 have been used on the LHS and RHS, respectively. A neutral mass density of $1.34 \times 10^{-8} \text{ g/cm}^3$ (corresponding to a kinematic viscosity of $\sim 0.87 \text{ m}^2/\text{s}$), an N_2 atmosphere has been assumed, water cluster ions were assumed to have a mass of 91 amu ($H^+(H_2O)_5$), and a neutral temperature of $T_n = 150 \text{ K}$ were used in these calculations.

model, so that D_A/D_i , the ratio of the aerosol to water cluster ion diffusion coefficients, is $\sim 4.3 \times 10^{-19} r_A^{-2}$ where r_A is the aerosol particle size in meters (Cho et al., 1992a). The resulting diffusion of electrons is characterized by a “fast” diffusion mode (D_1 in the literature) and a “slow” diffusion mode (D_2). As discussed in the introduction, Rapp and Lübken (2003) showed that initially electron irregularities diffuse with the fast diffusion mode, D_1 , but very quickly transition to the slow diffusion mode, D_2 , so that the electron fluctuation level decays to only ~ 0.5 of its initial value at the D_1 diffusion rate. Thus, for the purposes of this paper, we will assume the most favorable condition, that the electron fluctuations decay at the slow diffusion rate, which is the same approach taken by La Hoz et al. (2006), although clearly this is an oversimplification.

Using typical values at 82 km obtained from the MSIS-90 model (Hedin, 1991) (see caption), we have computed the slow diffusion rates, D_2 , as a function of the fraction of charge in the aerosols for two different charge numbers, $Z_A = -1$ and -5 , and particle sizes from 10 to 30 nm, which are plotted in the top panels of Fig. 10. The latter charge number of -5 can be considered close to an upper limit, based on both measurements and models (e.g., Rapp and Lübken, 2001), and we note that positively charged ice would also enhance the Schmidt number. For reference, the dashed lines in these plots correspond to the fast diffusion rates, D_1 , scaled by a factor of 1000. This curve is essentially independent of aerosol size (e.g., Rapp and Lübken, 2003). The lower panels of Fig. 10 show the diffusion times on the right axis, calculated as $\tau = (D_2 k^2)^{-1}$, and the corresponding Schmidt number on the left axis (the two quantities are proportional to each other). These quantities vary in proportion to the square of the aerosol particle size. Slow diffusion times are in the range of seconds for the singly charged case to tens of seconds for the multiply charged case. For reasonable experimentally measured values of $|Z_A|N_A/N_e$ of ~ 0.1 – 0.2 (Havnes et al., 2001; Blix et al., 2003), we can see that larger particles, >20 – 30 nm, or multiply charged particles of smaller size (~ 15 – 20 nm) can produce the required Schmidt numbers,

even for the worst case, narrowest spectra. In addition, the irregularities imposed by these large particles acquire longer diffusion times and can thus persist if the turbulent source is turned off, at least for a short time. These results are consistent with observations of PMSE at relatively low altitudes as compared to lower frequency observations, which typically peak at 85–90 km (e.g., Rapp and Lübken, 2004). Larger particles sediment downwards and thus one would expect PMSE at smaller scales to occur, on the average, at lower altitudes if they are associated with larger particles that enhance the Schmidt number and increase the diffusion time of the electron density irregularities.

Thus, it appears that turbulence can indeed explain the presence of electron irregularities at UHF, even for the narrow spectral widths, whose interpretation may be more difficult (see statement at the end of the previous subsection). We emphasize the sensitivity of this calculation to the neutral density, to which the ion diffusion rate is inversely proportional. The neutral density changes by a factor of 2 within 5 km at these altitudes, with higher densities leading to longer diffusion times. Note that the Schmidt number does not depend on the neutral density since the coefficient of kinematic viscosity is also inversely proportional to ρ .

5. Conclusion

In this paper, we have presented the first spectral observations of PMSE with the 450-MHz PFISR, which is sensitive to fluctuations at a 33 cm Bragg wavelength. PMSE at these wavelengths are much rarer than longer wavelengths because of required Schmidt numbers and turbulence energy dissipation rates. The PMSE presented here occurred at night during auroral particle precipitation, which enhanced the background D -region. The observations reveal two classes of spectra associated with PMSE at UHF, at least for this single day of observations: a relatively rare, broad class of spectra with spectral widths (rms velocity

fluctuations) up to 10 m/s, and a much more common, narrow class of spectra, with rms velocity fluctuations near 1 m/s. The broad echoes, whose widths are characteristic of a more turbulent source, show time and spatial variations indicative of a turbulent environment. It has thus been postulated that these echoes occur with active neutral air turbulence occurring within the radar field-of-view. The presence of active turbulence requires lower Schmidt numbers for extension of the inertial-convective subrange, which could explain why these echoes are rare: they are associated with smaller particles, have larger diffusion coefficients, and thus diffuse away more quickly; thus, they require the existence of neutral turbulence within or very close to the beam. The narrow echoes, on the other hand, have longer diffusion times and can become entrained in the wind, thus explaining the comparatively consistent time and spatial features of these echoes. We find that the Schmidt numbers required to explain these narrow features are high, several thousand, but are within reason in light of the Rapp and Lübken (2003) theory. Even so, such Schmidt numbers may not be necessary because of the likely spectral evolution that takes place as the turbulent source dies away—namely, a transitioning to narrower spectra.

While we have not discussed the charging mechanism for the ice particles, we postulate that whether or not ice becomes positively or negatively charged depends on the relative importance of photoemission versus electron collection. One would expect impact ionization from auroral particle precipitation to charge ice positive; on the other hand, electron collection from an enhanced *D*-region plasma would charge the ice negative (Goertz, 1989). In a future study, we plan to investigate these effects quantitatively using derived electron energy spectra from the background density measurements.

Acknowledgments

The PFISR was developed under NSF cooperative agreement ATM-0121483, and the data collection and analysis was supported under NSF cooperative agreement ATM-0608577. Work at Cornell University was supported by NSF grant ATM-0538343.

References

- Balsley, B.B., Ecklund, W.L., Fritts, D.C., 1983. Mesospheric radar echoes at Poker Flat, Alaska: evidence for seasonally dependent generation mechanisms. *Radio Science* 18, 1053–1058.
- Batchelor, G.K., 1959. Small-scale variation of convected quantities like temperature in turbulent fluid. Part 1: general discussion and the case of small conductivity. *Journal of Fluid Mechanics* 5, 113–133.
- Blix, T.A., Rapp, M., Lübken, F.J., 2003. Relations between small scale electron number density fluctuations, radar backscatter, and charged aerosol particles. *Journal of Geophysical Research* 108 (D8), 8450.
- Cho, J.Y.N., Kelley, M.C., 1993. Polar mesosphere summer radar echoes. *Reviews of Geophysics* 31, 243–265.
- Cho, J.Y.N., Röttger, J., 1997. An updated review of polar mesosphere summer echoes: observation, theory, and their relationship to noctilucent clouds and subvisible aerosols. *Journal of Geophysical Research* 102, 2001–2020.
- Cho, J.Y.N., Hall, T.M., Kelley, M.C., 1992a. On the role of charged aerosols in polar mesosphere summer echoes. *Journal of Geophysical Research* 97, 875–886.
- Cho, J.Y.N., Kelley, M.C., Heinselman, C.J., 1992b. Enhancement of Thomson scatter by charged aerosols in the polar mesosphere: measurements with a 1.29 GHz radar. *Geophysical Research Letters* 19, 1097–1100.
- Czechowsky, P., Rüster, R., Schmidt, G., 1979. Variations of mesospheric structures in different seasons. *Geophysical Research Letters* 6, 459–462.
- Ecklund, W.L., Balsley, B.B., 1981. Long term observations of the arctic mesosphere with the MST radar at Poker Flat, Alaska. *Journal of Geophysical Research* 86, 7775–7780.
- Fritts, D.C., Hoppe, U.-P., Inhester, B., 1990. A study of the vertical motion field near the high-latitude summer mesopause during MAC/SINE. *Journal of Atmospheric and Terrestrial Physics* 52, 927–938.
- Garcia, R.R., Solomon, S., 1985. Effect of breaking gravity waves on the dynamics and chemical composition of the mesosphere and lower thermosphere. *Journal of Geophysical Research* 90 (D2), 3850–3868.
- Gibson-Wilde, D., Werne, J., Fritts, D., Hill, R., 2000. Direct numerical simulation of VHF radar measurements of turbulence in the mesosphere. *Radio Science* 35 (3), 783–798.
- Goertz, C., 1989. Dusty plasmas in the solar system. *Reviews of Geophysics* 27 (2), 271–292.
- Hall, C.M., Röttger, J., 2001. Initial observations of polar mesospheric summer echoes using the EISCAT Svalbard Radar. *Geophysical Research Letters* 28, 131–134.
- Havnes, O., Troim, J., Blix, T., Mortensen, W., Naesheim, L.I., Thrane, E., Tonnesen, T., 1996. First detection of charged dust particles in the Earth's mesosphere. *Journal of Geophysical Research* 101 (A5), 10839–10847.
- Havnes, O., Brattli, A., Aslaksen, T., Singer, W., Latteck, R., Blix, T., Thrane, E., Troim, J., 2001. First common volume observations of layered plasma structures and polar mesospheric summer echoes by rocket and radar. *Geophysical Research Letters* 28 (8), 1419–1422.
- Hedin, A.E., 1991. Extension of the MSIS thermosphere model into the middle and lower atmosphere. *Journal of Geophysical Research* 96, 1159–1172.
- Hill, R.J., 1978. Nonneutral and quasi-neutral diffusion of weakly ionized multi-constituent plasma. *Journal of Geophysical Research* 83, 989–998.
- Hill, R.J., Clifford, S.F., 1978. Modified spectrum of atmospheric temperature fluctuations and its application to optical propagation. *Journal of the Optical Society of America* 68, 892–899.
- Hill, R.J., Gibson-Wilde, D.E., Werne, J.A., Fritts, D.C., 1999. Turbulence-induced fluctuations in ionization and application to PMSE. *Earth Planets and Space* 51, 499–513.
- Hocking, W.K., 1983. On the extraction of atmospheric turbulence parameters from radar backscatter Doppler spectra. *Journal of Atmospheric and Terrestrial Physics* 45, 89–102.
- Hocking, W.K., 1985. Measurement of turbulent energy dissipation rates in the middle atmosphere by radar techniques: a review. *Radio Science* 20 (6), 1403–1422.
- Hocking, W.K., 1988. Two years of continuous measurements of turbulence parameters in the upper mesosphere and lower thermosphere made with a 2-MHz radar. *Journal of Geophysical Research* 93, 2475–2491.
- Hocking, W.K., 1996. An assessment of the capabilities and limitations of radars in measurements of upper atmosphere turbulence. *Advances in Space Research* 17 (11), 37–47.
- Hoppe, U.-P., Fritts, D.C., 1995. High-resolution measurements of vertical velocity with the European incoherent scatter VHF radar 1. Motion field characteristics and measurement biases. *Journal of Geophysical Research* 100 (D8), 16813–16825.
- Hoppe, U.-P., Hall, C., Röttger, J., 1988. First observations of summer polar mesospheric backscatter with a 224 MHz radar. *Geophysical Research Letters* 15, 28–31.
- Kelley, M.C., Farley, D.T., Röttger, J., 1987. The effect of cluster ions on anomalous VHF backscatter from the summer polar mesosphere. *Geophysical Research Letters* 14, 1031–1034.
- La Hoz, C., Havnes, O., 2007. Can charged dust explain polar mesospheric summer echoes? Theory and experiments. *Eos Transactions of the AGU* 88(52), Fall Meeting Supplement, Abstract SA21A-0247.
- La Hoz, C., Havnes, O., Naesheim, L.I., Hysell, D.L., 2006. Observations and theories of polar mesospheric summer echoes at a Bragg wavelength of 16 cm. *Journal of Geophysical Research* 111, D04203.
- Lehtinen, M.S., Dantie, B., Nygren, T., 2004. Optimal binary phase codes and sidelobe-free decoding filters with application to incoherent scatter radar. *Annales de Geophysique* 22, 1623–1632.
- Lübken, F.-J., 1997. Seasonal variation of turbulent energy dissipation rates at high latitudes as determined by in situ measurements of neutral density fluctuations. *Journal of Geophysical Research* 102, 13441–13456.
- Lübken, F.-J., 1999. Thermal structure of the Arctic summer mesosphere. *Journal of Geophysical Research* 104, 9135–9149.
- Lübken, F.-J., Lehmacher, G., Blix, T., Hoppe, U.-P., Thrane, E., Cho, J., Swartz, W., 1993. First in-situ observations of neutral and plasma density fluctuations within a PMSE layer. *Geophysical Research Letters* 20, 2311–2314.
- Lübken, F.-J., Rapp, M., Hoffmann, P., 2002. Neutral air turbulence and temperatures in the vicinity of polar mesosphere summer echoes. *Journal of Geophysical Research* 107, 4273.
- Mitchell, J.D., Croskey, C.L., Goldberg, R.A., 2001. Evidence for charged aerosols and associated meter-scale structure in identified PMSE/NLC regions. *Geophysical Research Letters* 28 (8), 1423–1426.
- Nicolls, M.J., Heinselman, C.J., Hope, E.A., Ranjan, S., Kelley, M.C., Kelly, J.D., 2007. Imaging of polar mesosphere summer echoes with the 450-MHz Poker Flat Advanced Modular Incoherent Scatter Radar. *Geophysical Research Letters* 34, L21012.
- Pedersen, A., Troim, J., Kane, J.A., 1969. Rocket measurements showing removal of electrons above the mesopause in summer at high latitude. *Planetary and Space Science* 18, 945–947.
- Rapp, M., Hoppe, U.-P., 2006. A reconsideration of spectral width measurements in PMSE with EISCAT. *Advances in Space Research* 38, 2408–2412.
- Rapp, M., Lübken, F.-J., 2001. Modelling of particle charging in the polar summer mesosphere: part 1—general results. *Journal of Atmospheric and Solar-Terrestrial Physics* 63, 759–770.
- Rapp, M., Lübken, F.-J., 2003. On the nature of PMSE: electron diffusion in the vicinity of charged particles revisited. *Journal of Geophysical Research* 108, 8437.

- Rapp, M., Lübken, F.-J., 2004. Polar mesosphere summer echoes (PMSE): review of observations and current understanding. *Atmospheric Chemistry and Physics* 4, 2601–2633.
- Rapp, M., Gumbel, J., Lübken, F.-J., Latteck, R., 2002. D region electron number density limits for the existence of polar mesosphere summer echoes. *Journal of Geophysical Research* 107 (D14).
- Rapp, M., Lübken, F.-J., Hoffmann, P., Latteck, R., Baumgarten, G., Blix, T.A., 2003. PMSE dependence on aerosol charge number density and aerosol size. *Journal of Geophysical Research* 108, 8441.
- Rapp, M., Strelnikova, I., Latteck, R., Hoffman, P., Hoppe, U.-P., Häggström, I., Rietveld, M.T., 2008. Polar mesosphere summer echoes (PMSE) studied at Bragg wavelengths of 2.8 m, 67 cm, and 16 cm. *Journal of Atmospheric and Solar-Terrestrial Physics* 70, 947–961.
- Rastogi, P.K., Bowhill, S.A., 1976. Scattering of radio waves from the mesosphere. 1. Theory and observations. *Journal of Atmospheric and Terrestrial Physics* 38, 399–411.
- Reid, G.C., 1990. Ice particles and electron 'bite-outs' at the summer polar mesopause. *Journal of Geophysical Research* 95, 13891–13896.
- Röttger, J., La Hoz, C., 1990. Characteristics of polar mesosphere summer echoes (PMSE) observed with the EISCAT 224 MHz radar and possible explanations of their origin. *Journal of Atmospheric and Terrestrial Physics* 52, 893–906.
- Röttger, J., Hoz, C.L., Kelley, M.C., Hoppe, U.P., Hall, C., 1988. The structure and dynamics of polar mesosphere summer echoes observed with the EISCAT 224 MHz radar. *Geophysical Research Letters* 15, 1353–1356.
- Röttger, J., Rietveld, M.T., La Hoz, C., Hall, C., Kelley, M.C., Swartz, W.E., 1990. Polar mesosphere summer echoes observed with the EISCAT 933-MHz radar and the CUPRI 469-MHz radar, their similarity to 224-MHz radar echoes, and their relation to turbulence and electron density profiles. *Radio Science* 25, 671–687.
- Sulzer, M.P., 1989. Recent incoherent scatter techniques. *Advances in Space Research* 9, 153–162.
- Ulwick, J.C., Baker, K.D., Kelley, M.C., Balsley, B.B., Ecklund, W.L., 1988. Comparison of simultaneous MST radar and electron density probe measurements during STATE. *Journal of Geophysical Research* 93, 6989–7000.
- Varney, R.H., Nicolls, M.J., Heinselman, C.J., Kelley, M.C., 2008. Observations of polar mesospheric summer echoes using PFISR during the summer of 2007. *Journal of Atmospheric and Solar-Terrestrial Physics*, submitted for publication.
- Weinstock, J., 1981. Energy dissipation rates of turbulence in the stable free atmosphere. *Journal of the Atmospheric Sciences* 38, 880–883.
- Werne, J., Fritts, D.C., 1999. Stratified shear turbulence: evolution and statistics. *Geophysical Research Letters* 26, 439–442.